Computational Mechanics
https://doi.org/10.1007/s00466-023-02341-8

ORIGINAL PAPER

Revealing aeroelastic effects on low-rise roof structures in turbulent winds via isogeometric fluid–structure interaction

Qiming Zhu[1,2] · Xuguang Wang[3,4] · Cristoforo Demartino[3,4] · Jinhui Yan[4]

Received: 13 February 2023 / Accepted: 5 April 2023

Abstract
Aeroelastic effects, which affect the dynamic responses of low-rise roof structures to extreme wind conditions, are often neglected or oversimplified in current wind engineering design standards and applications. However, it is crucial to understand the details of those aeroelastic effects for performance-based wind engineering. This paper presents an isogeometric fluid–structure interaction (FSI) tool to investigate the aeroelastic effects of wind pressure distributions on roof structures under different turbulent wind conditions. A representative low-rise roof structure is simulated with an FSI model using an Arbitrary Lagrange-Eulerian-based variational multi-scale formulation coupled with isogeometric Kirchhoff-Love shells. The simulation results are compared to the quasi-steady approach and wind load provisions from ASCE 7-22. It shows that the quasi-steady approach and the design standard underestimate the pressure fluctuations, indicating the necessity of using FSI simulations to capture the aeroelastic effect for the roof of low-rise structures. This paper also studies the impacts of different roof configurations, e.g., the number of roof panels and inflow turbulent intensity, on the distribution of pressure coefficients and roof deflections. For the given mean wind speed, the mean pressure coefficient remains almost the same regardless of the turbulent intensity and roof configuration. However, the pressure fluctuation (standard deviation) varies significantly with the turbulence intensity and roof configuration. The aeroelastic effect also leads to complicated roof deflections at the crucial location having the maximum pressure coefficient. The paper first describes the mathematical details of the FSI model and simulation setup. Then, the pressure coefficients by the FSI simulation and design code are compared. Finally, the roof deflection with different inlet turbulence intensities and roof configurations are presented and discussed.

Keywords FSI · Civil structures · IGA

1 Introduction

Widely adopted in coastal areas of the USA, low-rise structures represent one of the most vulnerable structures under extreme wind events and are the largest source of direct and indirect damage and fatality. Nowadays, the wind engineering community is moving towards performance-based design to increase urban resilience [1]. Design standards, such as ASCE 7-22 [2], provide prescriptive guidelines for calculating the pressure on the roof of low-rise structures. However, more accurate predictions on the uplifting pressure are required for performance-based wind engineering. Research into low-rise structures and their interaction with turbulent winds is vital for predicting, responding to, and mitigating threats of extreme wind events to our community. Due to the systematic, repeatable, controllable boundary conditions of the low-rise structures, numerical models based on

✉ Xuguang Wang
xuguangw@illinois.edu

✉ Jinhui Yan
yjh@illinois.edu

[1] Key Lab of Structures Dynamic Behavior and Control of the Ministry of Education, Harbin Institute of Technology, Harbin, People's Republic of China

[2] Key Lab of Smart Prevention and Mitigation of Civil Engineering Disasters of the Ministry of Industry and Information Technology, Harbin Institute of Technology, Harbin, People's Republic of China

[3] University of Illinois at Urbana Champaign Institute, Zhejiang University , Haining, Zhejiang, People's Republic of China

[4] Department of Civil and Environmental Engineering, University of Illinois at Urbana-Champaign, Champaign, IL, USA

Published online: 03 May 2023

computational fluid dynamics (CFD) are frequently used to estimate wind pressure loads for more effective designs.

Many wind tunnel experiments have indicated the importance of structure's aeroelastic behaviors [3] on wind pressure distributions. A recent study in Florida International University's Wall of Wind experimental facility [4] found that the membrane deformation of flexible roofs can result in a significant reduction of peak pressure coefficients as compared to those of rigid roofs. However, these aeroelastic effects are neither thoroughly investigated nor accounted for in most of the current wind engineering models to determine the wind-induced pressure distributions. These CFD models, including Reynolds-averaged Navier-Stokes (RANS) and large-eddy simulations (LES), often neglect the aeroelastic efforts or employ oversimplified approaches. High-fidelity fluid–structure interaction (FSI) simulations of low-rise roof structures are still limited due to the large Reynolds number of wind flows and complicated interaction between wind and structures.

This paper presents a general high-fidelity FSI model and deploys it to representative low-rise roof structures to investigate the aeroelastic effects on wind pressure distribution and roof deflections. For fluid mechanics, the FSI model uses a residual-based variational multi-scale formulation (VMS) to capture high Reynolds number wind flows. RBVMS, as a variationally-consistent LES turbulence model, aims to capture the spatiotemporal details of large Reynolds number wind turbulence [5]. A boundary-fitted moving domain CFD technique based on arbitrary Lagrangian–Eulerian (ALE) is utilized to handle the deformation of the fluid–structure interface. For structural mechanics, the FSI model utilizes isogeometric analysis (IGA)-based Kirhhoff-Love shells to discretize the roof structure. IGA aims to integrate design and analysis by directly employing the spline functions of computer-aided design (CAD) models to perform engineering analysis [6, 7]. Besides, due to the higher-order basis functions, IGA attains exact geometry descriptions of structures and has been proven to have higher accuracy per degree of freedom than traditional finite element methods using Lagrangian polynomial basis functions. The integration of ALE, VMS, and IGA (isogeometric ALE-VMS) leads to a high-fidelity predictive FSI model suitable for wind engineering applications considered in this paper. The isogeometric ALE-VMS FSI model has been widely validated by a set of benchmark problems and realistic problems in wind energy [8–11], which share several similarities with the wind engineering problem considered here from the perspective of aerodynamics. A set of parametric studies is carried out to demonstrate the aeroelastic effects on roofs with different stiffness under various inflow turbulence conditions.

The paper is structured as follows. Section 2 introduces the high-fidelityi FSI model, including governing equations of fluid and structural dynamics and the isogeometric ALE-VMS methodology. The details of the setup of FSI simulations of roof structures are shown in Sect. 3. Then, the FSI simulation results are presented and compared to the pressure coefficients suggested by ASCE 7-22 in Sect. 4. Lastly, Sect. 5 draws the conclusions.

2 FSI formulation

2.1 Governing equations

Let Ω_f, Ω_s, and Γ_I denote the fluid domain, structural domain, and fluid–structure interface, respectively. The strong form governing equations of the FSI model are given as

$$\rho_f \left[\frac{\partial \boldsymbol{u}}{\partial t} + \left(\boldsymbol{u} - \hat{\boldsymbol{u}}\right) \cdot \nabla \boldsymbol{u} - \boldsymbol{f}_f \right] - \nabla \cdot \boldsymbol{\sigma}_f = \boldsymbol{0} \quad \text{in } \Omega_f \tag{1}$$

$$\nabla \cdot \boldsymbol{u} = 0 \quad \text{in } \Omega_f \tag{2}$$

$$\rho_s \left(\frac{d^2 \boldsymbol{y}}{dt^2} - \boldsymbol{f}_s \right) - \nabla \cdot \boldsymbol{\sigma}_s = \boldsymbol{0} \quad \text{in } \Omega_s \tag{3}$$

$$\boldsymbol{u} = \frac{d \boldsymbol{y}}{dt} \quad \text{in } \Gamma_I \tag{4}$$

$$\boldsymbol{\sigma}_f \boldsymbol{n}_f + \boldsymbol{\sigma}_s \boldsymbol{n}_s = \boldsymbol{0} \quad \text{in } \Gamma_I \tag{5}$$

where Eq. 1 and Eq. 2 are the Navier-Stokes equations of incompressible flows, in which ρ_f is the fluid density, $\boldsymbol{u}$ is the fluid velocity, $\boldsymbol{f}_f$ is the fluid body force per unit mass, $\boldsymbol{\sigma}_f = -p\boldsymbol{I} + 2\mu\nabla^s \boldsymbol{u}$ is the fluid Cauchy stress tensor, where p is the fluid pressure, μ is the dynamics viscosity, ∇^s is the symmetric gradient operator, and $\boldsymbol{I}$ is a 3×3 identity matrix. Equation 3 is the conversation law of linear momentum of structural mechanics, in which ρ_s is the structural density, $\boldsymbol{y}$ is the structural displacement, $\boldsymbol{f}_s$ is the structural body force per unit mass, and $\boldsymbol{\sigma}_s$ is the structural Cauchy stress tensor. At last, Eq. 4 and Eq. 5 are the kinematics and traction compatibility on the fluid–structure interface, in which $\boldsymbol{n}_f$ and $\boldsymbol{n}_s$ represent the unit normal vectors of on the fluid–structure interface ($\boldsymbol{n}_f = -\boldsymbol{n}_s$). One should note that the structural equation is imposed on a Lagrangian description, while the fluid equations are imposed on a moving domain through an ALE technique with $\hat{\boldsymbol{u}}$ representing the mesh velocity.

2.2 Isogeometric thin shell theory

Since the roof structure considered in this paper is essentially a thin shell, the Kirchhoff-Love shell kinematics theory is introduced into the weak formulation (or Galerkin formulation) of the structural mechanics equation (Eq. 3) to save computational cost. Furthermore, the structure is assumed to obey the St. Venant-Kirchhoff material law. As a result, a thin shell formulation, written purely in terms of the roof's

mid-surface displacements, is obtained. The shell formulation is also referred to as "rotation-free" [12] compared with Reissner-Mindlin shell theory. The shell formulation is discretized by isogeometric analysis (IGA) using second-order Non-Uniform Rational B-Splines (NURBS) [6]. The weak formulation of the rotation-free isogeometric shell is stated as: Find the shell mid-surface displacement $\boldsymbol{y} \in \mathcal{V}_s$ such that for $\forall \boldsymbol{w}_s \in \mathcal{W}_s$

$$B^s(\boldsymbol{w}_s, \boldsymbol{y}) - F^s(\boldsymbol{w}_s) = 0 \tag{6}$$

where

$$B^s(\boldsymbol{w}_s, \boldsymbol{y}) = \int_{A_s} \boldsymbol{w}_s \cdot \overline{\rho}_s h \frac{\partial^2 \boldsymbol{y}}{\partial t^2} d\Omega \tag{7}$$

$$+ \int_{A_s} \delta\boldsymbol{\varepsilon}(\boldsymbol{w}_s) \left[\boldsymbol{K}_{mem} \boldsymbol{\varepsilon}(\boldsymbol{y}) + \boldsymbol{K}_{coup} \boldsymbol{\kappa}(\boldsymbol{y}) \right] dA \tag{8}$$

$$+ \int_{A_s} \delta\boldsymbol{\kappa}(\boldsymbol{w}_s) \left[\boldsymbol{K}_{coup} \boldsymbol{\varepsilon}(\boldsymbol{y}) + \boldsymbol{K}_{bend} \boldsymbol{\kappa}(\boldsymbol{y}) \right] dA \tag{9}$$

and

$$F^s(\boldsymbol{w}_s) = \int_{A_s} \boldsymbol{w}_s \cdot \overline{\rho}_s h \boldsymbol{f}_s d\Omega + \int_{\Gamma_s^{\mathrm{N}}} \boldsymbol{w}_s \cdot \boldsymbol{h}_s \, d\Gamma \tag{10}$$

In the above formulation, $\mathcal{W}_s$ and $\mathcal{V}_s$ denote the test and trial function sets for the structural mechanics equations. h is the thickness of the roof, A_s denotes the middle surface, $\boldsymbol{\varepsilon}(\boldsymbol{y})$ and $\boldsymbol{\kappa}(\boldsymbol{y})$ are the tensors of the roof membrane strains and curvature changes expressed in Voigt notation and written with respect to the local basis oriented on the first covariant basis vector of the roof mid-surface. $\delta\boldsymbol{\varepsilon}(\boldsymbol{w}_s)$ and $\delta\boldsymbol{\kappa}(\boldsymbol{w}_s)$ are the corresponding variations. $\boldsymbol{h}_s$ is the applied traction on the roof surface. $\boldsymbol{K}_{mem}$, $\boldsymbol{K}_{coup}$, and $\boldsymbol{K}_{bend}$ are the membrane, coupling, and bending stiffness, respectively, which are defined as

$$\boldsymbol{K}_{mem} = \int_{-h/2}^{h/2} \boldsymbol{C} dz \tag{11}$$

$$\boldsymbol{K}_{coup} = \int_{-h/2}^{h/2} \boldsymbol{C} z dz \tag{12}$$

$$\boldsymbol{K}_{bend} = \int_{-h/2}^{h/2} \boldsymbol{C} z^2 dz \tag{13}$$

where $\boldsymbol{C}$ is defined as

$$\boldsymbol{C} = \begin{bmatrix} \frac{E}{1-\nu^2} & \frac{\nu E}{1-\nu^2} & 0 \\ \frac{\nu E}{1-\nu^2} & \frac{E}{1-\nu^2} & 0 \\ 0 & 0 & G \end{bmatrix} \tag{14}$$

where E, G, and ν are Young's modulus, shear modulus, and Poisson's ratio of the structural material, respectively.

2.3 ALE-VMS for fluid mechanics

This paper adopts an ALE-VMS approach to solve fluid mechanics equations. The weak formulation is stated as: Find $\{\boldsymbol{u}, p\} \in \mathcal{V}_f$ such that $\forall \{\boldsymbol{w}_f, q\} \in \mathcal{W}_f$

$$B^f\left(\{\boldsymbol{w}_f, q\}, \{\boldsymbol{u}, p\}\right) - F^f\left(\{\boldsymbol{w}_f, q\}\right) = 0 \tag{15}$$

where $B^f\left(\{\boldsymbol{w}_f, q\}, \{\boldsymbol{u}, p\}\right)$ and $F^f\left(\{\boldsymbol{w}_f, q\}\right)$ are defined as

$$\begin{aligned} B^f&\left(\{\boldsymbol{w}_f, q\}, \{\boldsymbol{u}, p\}\right) \\ &= \int_{\Omega_f} \boldsymbol{w}_f \cdot \rho_f \left[\frac{\partial \boldsymbol{u}}{\partial t} + (\boldsymbol{u} - \hat{\boldsymbol{u}}) \cdot \nabla \boldsymbol{u} \right] d\Omega_f \\ &+ \int_{\Omega_f} q \, \nabla \cdot \boldsymbol{u} \, d\Omega_f \\ &+ \int_{\Omega_f} \nabla \boldsymbol{w}_f^S : \boldsymbol{\sigma}_f(\boldsymbol{u}, p) \, d\Omega_f \\ &- \sum_{e=1}^{N_{el}} \int_{\Omega^f} \left[(\boldsymbol{u} - \hat{\boldsymbol{u}}) \cdot \nabla \boldsymbol{w}_f + \frac{\nabla q}{\rho_f} \right] \cdot \boldsymbol{u}' \, d\Omega_f \\ &- \sum_{e=1}^{N_{el}} \int_{\Omega^f} p' \nabla \cdot \boldsymbol{w}_f \, d\Omega_f \\ &+ \sum_{e=1}^{N_{el}} \int_{\Omega^f} \boldsymbol{w}_f \cdot (\boldsymbol{u}' \cdot \nabla \boldsymbol{u}) \, d\Omega_f \\ &- \sum_{e=1}^{N_{el}} \int_{\Omega^f} \frac{\nabla \boldsymbol{w}_f}{\rho_f} : (\boldsymbol{u}' \otimes \boldsymbol{u}') \, d\Omega_f \end{aligned} \tag{16}$$

and

$$F^f\left(\{\boldsymbol{w}_f, q\}\right) = \int_{\Omega_f} \boldsymbol{w}_f \cdot \rho_f \boldsymbol{f}_f \, d\Omega_f + \int_{\Gamma_f^{\mathrm{N}}} \boldsymbol{w}_f \cdot \boldsymbol{h}_f \, d\Gamma \tag{17}$$

In the above formulation, $\mathcal{W}_f$ and $\mathcal{V}_f$ denote the test and trial function sets for the fluid mechanics equations. $\boldsymbol{h}_f$ is the fluid traction applied on Γ_f^{N} ($\Gamma_f^{\mathrm{N}} \subset \partial\Omega^f$). All the integrals of B^f computed in an element-wise fashion correspond to the fine-scale terms stemming from the residual-based variational multi-scale formulation (VMS). In these terms, e is the element count and N_{el} is the total number of elements. The fine-scale velocity $\boldsymbol{u}'$ and fine-scale pressure p' are defined as

$$\boldsymbol{u}' = -\tau_{\mathrm{M}} \left\{ \rho_f \left[\frac{\partial \boldsymbol{u}}{\partial t} + (\boldsymbol{u} - \hat{\boldsymbol{u}}) \cdot \nabla \boldsymbol{u} - \boldsymbol{f}_f \right] - \nabla \cdot \boldsymbol{\sigma}_f(\boldsymbol{u}, p) \right\} \tag{18}$$

$$p' = -\rho_f \tau_C \nabla \cdot \boldsymbol{u} \tag{19}$$

where τ_M and τ_C are corresponding stabilization parameters based on streamline upwind Petrov-Galerkin (SUPG), pressure-stabilizing Petrov-Galerkin (PSPG), and Least Square on Incompressibility constraint (LSIC). More details about their definitions can be found in [5, 13–15].

2.4 FSI formulation

The above finite element and IGA formulations for fluid and structural mechanics feature a non-matching FSI approach, similar to those applied to wind turbine simulations [16]. The final FSI formulation can be stated as: Find $\{\boldsymbol{u}, p\} \in \mathcal{V}_f$ and $\boldsymbol{y} \in \mathcal{V}_s$ such that $\forall \{\boldsymbol{w}_f, q\} \in \mathcal{W}_f$ and $\boldsymbol{w}_s \in \mathcal{W}_s$

$$\begin{aligned} &B^f\left(\{\boldsymbol{w}_f, q\}, \{\boldsymbol{u}, p\}\right) - F^f\left(\{\boldsymbol{w}_f, q\}\right) + B^s\left(\boldsymbol{w}_s, \boldsymbol{y}\right) - F^s\left(\boldsymbol{w}_s\right) \\ &- \int_{\Gamma_I} \left(\boldsymbol{w}_f - \boldsymbol{w}_s\right) \cdot \boldsymbol{\sigma}_f\left(\boldsymbol{u}, p\right) \boldsymbol{n}_f \, d\Gamma \\ &- \int_{\Gamma_I} \left[\delta_{\{\boldsymbol{u},p\}} \boldsymbol{\sigma}_f \boldsymbol{n}_f\left(\{\boldsymbol{w}_f, q\}\right)\right] \cdot \left(\boldsymbol{u}_f - \frac{d\boldsymbol{y}}{dt}\right) d\Gamma \\ &+ \int_{\Gamma_I} \left(\boldsymbol{w}_f - \boldsymbol{w}_s\right) \cdot \beta \left(\boldsymbol{u}_f - \frac{d\boldsymbol{y}}{dt}\right) d\Gamma = 0 \end{aligned} \tag{20}$$

The above formulation belongs to a family of an augmented Lagrangian approach for coupled problems parameterized by β.

2.5 Coupling strategy and other numerical details

The above FSI formulation is solved in a block-iterative approach, with equations as given by or similar to those in Section 5.1 in [17] and Section 5.1 in [18]. Besides, a weakly-enforced no-slip boundary condition [19, 20] is applied on the fluid–structure interface to relax the boundary-layer resolution without losing the accuracy of aerodynamic load prediction. The generalized-α method is used for the time integration. The Newton-Raphson method is used to linearize the nonlinear nodal equations. The resulting linear systems are solved by a generalized minimal residual method (GMRES) solver with a block-diagonal preconditioning. All the simulations presented next are carried out in parallel using Message Passing Interface (MPI) on the Stampede2 at the Texas Advanced Computing Center (TACC).

The FSI model presented in the paper comprises of a set of advanced numerical techniques for fluid and structural dynamics and their coupling. The IGA-based Kirchhoff–Love shell model plays a significant role in modeling thin-wall structures [21–25]. We should point out that IGA also shows great advantages in flow simulations [26–31]. VMS and its combinations with ALE (ALE-VMS) [32–38] and Space-Time (ST-VMS) technique [39–45], have successfully been employed as large eddy simulation (LES) models in simulating of a wide range of challenging CFD and FSI problems. These methods show significant advantages when being deployed to flow problems with moving interfaces and boundaries. Several recent validations and applications include environmental flows [20, 46–48], wind energy [8, 9, 11, 35, 49–65], tidal energy [63, 66–70], cavitation flows [71, 72], supersonic flows [73], bio-mechanics [74–80], gas turbine [81–83], and transportation engineering [84–89].

3 Computational FSI setup

This section introduces the computational FSI setup of the parametric study. The details of inflow turbulence generation are presented first, followed by the roof structure configurations and material definitions.

3.1 Inflow turbulence generation

Inflow turbulence is an important factor in wind engineering simulations. Despite its wide usage in many CFD/FSI simulations, uniform inflows are hardly seen in reality. In ASCE 7-22, the turbulence intensity is defined as a function of the equivalent height of the structure, $\bar{z}$, and an exposure type-based turbulence intensity factor, c, as:

$$I_{\bar{z}} = c\left(\frac{10}{\bar{z}}\right)^{1/6} \tag{21}$$

However, the effects caused by turbulence with this approach may be not sufficiently accurate for performance-based wind engineering designs. Thus, two numerical approaches, recycling/rescaling methods [90–93] and synthetic methods [94–96], are often adopted.

The recycling/rescaling methods need to perform auxiliary LES simulations, while the synthetic methods do not need and thus are computationally efficient. Because of this advantage, several synthetic methods, including synthetic random Fourier method [97], synthetic digital filtering method [98], and synthetic-eddy-method [96, 99, 100], have been proposed to generate artificial turbulent inflow conditions for wind engineering applications. Leveraging the authors' previous inflow model developed in [70], this paper employs a synthetic-eddy-method (SEM) based on a Lagrangian treatment of vortices to generate turbulent inflow conditions for the FSI simulations of roof structures in this paper. The inflow is assumed to consist of randomly distributed turbulent spots, and the spots are assumed to be convected downstream with provided velocity profile using Taylor's frozen turbulence hypothesis. The SEM approach is based on a superposition of different moving vortices. The velocity fluctuation at a point $\boldsymbol{x}$ that is influenced by N vor-

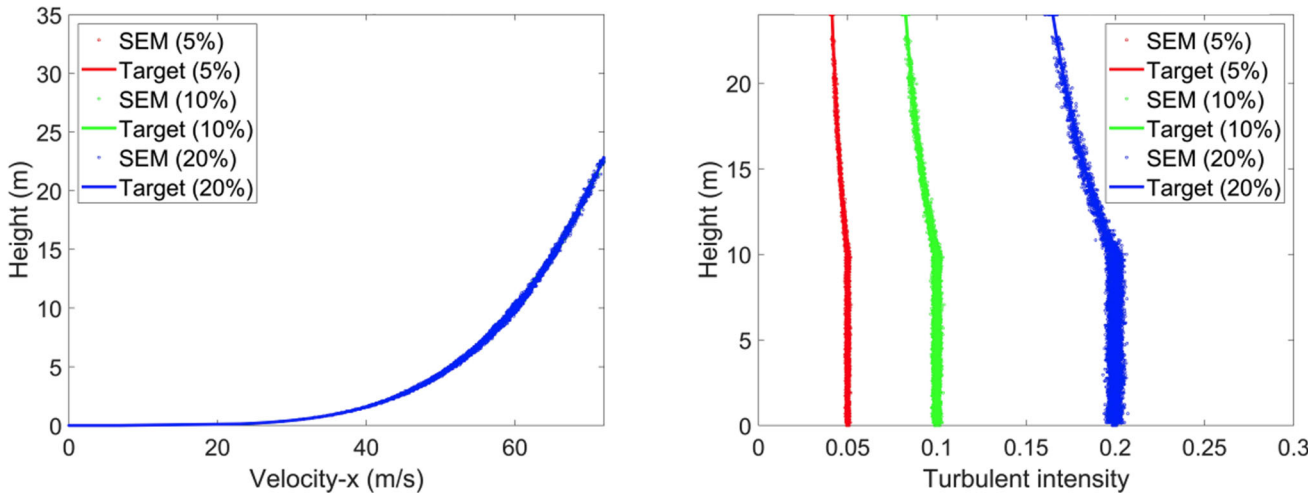

Fig. 1 Inflow wind profiles. *Left*: Mean flow. *Right*: Turbulent intensity

tices (or eddies) can be calculated by

$$\boldsymbol{u}_i'(\boldsymbol{x}) = \frac{1}{\sqrt{N}} \sum_{k=1}^{N} a_{ij} \sigma_j^k f_\sigma^k \left(\frac{\boldsymbol{x} - \boldsymbol{x}^k}{s^k} \right) \tag{22}$$

where $\boldsymbol{x}^k$ is the location of the k^{th} eddy, s^k is the length scale of the eddy obtained from an empirical formula, and $f_\sigma^k(\boldsymbol{x})$ is a so-called shape function. σ_j^k contains randomly assigned eddy intensities, which obey a Gaussian distribution with zero mean value and a standard deviation of 1. a_{ij} are the Lund coefficients related to the Reynolds stresses $R_{ij} = < \boldsymbol{u}_i' \boldsymbol{u}_j' >$, defined as

$$\boldsymbol{a} = \begin{bmatrix} \sqrt{R_{11}} & 0 & 0 \\ \frac{R_{21}}{a_{11}} & \sqrt{R_{22} - a_{21}^2} & 0 \\ \frac{R_{31}}{a_{11}} & \frac{R_{32} - a_{22} \cdot a_{31}}{a_{22}} & \sqrt{R_{33} - a_{31}^2 - a_{32}^2} \end{bmatrix} \tag{23}$$

In this paper, the mean profile and turbulent intensity of the wind profile are functions of height and are given as

$$u = u_r \left(\frac{z}{z_r} \right)^\alpha \tag{24}$$

$$I_u = \begin{cases} I_r & (z < z_r) \\ I_r \left(\frac{z}{z_r} \right)^{-\alpha} & (z \geq z_r) \end{cases} \tag{25}$$

where z is the height coordinate, z_r is a reference height, u_r and I_r are the mean wind velocity and turbulent intensity at z_r, and α is an empirical coefficient depending on the ground roughness and atmosphere stability. In this paper, u_r, z_r, and α are fixed to 60 m/s, 10 m, and 0.22, respectively. Three different turbulent intensities I_r = 5%, 10%, and 20% are generated by the above SEM approach. The generated mean and turbulent intensity profiles of the inflow wind conditions at several inlet locations are shown in Fig. 1.

3.2 Structural model

Figure 2 shows the geometry and dimensions of the roof structures considered in this paper. The roofs make use of homogeneous material, whose properties are summarized in Table 1. The roof structures are divided into multiple small panels to represent different roof-supporting systems. Shear connections (i.e., pinned boundary conditions) are assumed between the roof panels and the supporting truss structure. Due to the large stiffness of the supporting truss, it is assumed that there is no displacement on the boundary of each panel in the translational directions. Three different roof configurations of 4×4, 4×6, and 4×8 panels are considered in this paper. The panel stiffness in each configuration increases with the number of panels, hence increasing the overall roof stiffness. Due to the pinned boundary condition and high stiffness of the supporting truss, the displacement of a panel is not coupled with adjacent ones. The roof structures are discretized by second-order NURBS elements with 4,761 for the 4 × 4 case and 5,037 elements for the 4 × 6 and 4 × 8 cases. The fluid domain in the FSI simulations is a box with dimensions 55 m × 40 m × 24 m, and a refinement box with dimensions 45 m × 30 m × 10 m around the building is employed to better capture the bluff aerodynamics. The computational domain is discretized by tetrahedral elements in the interior and triangular prism elements in boundary layers around the structure surface and ground. We mesh the structure with a uniform grid with a length of 0.02 m. The height of the first boundary layer prism mesh is 0.002 m. The total number of nodes and elements of the mesh is 3,657,285 and 17,036,174, respectively. Figure 3 shows the fluid mesh on the x-z plane, y-z plane, and prism boundary layer near

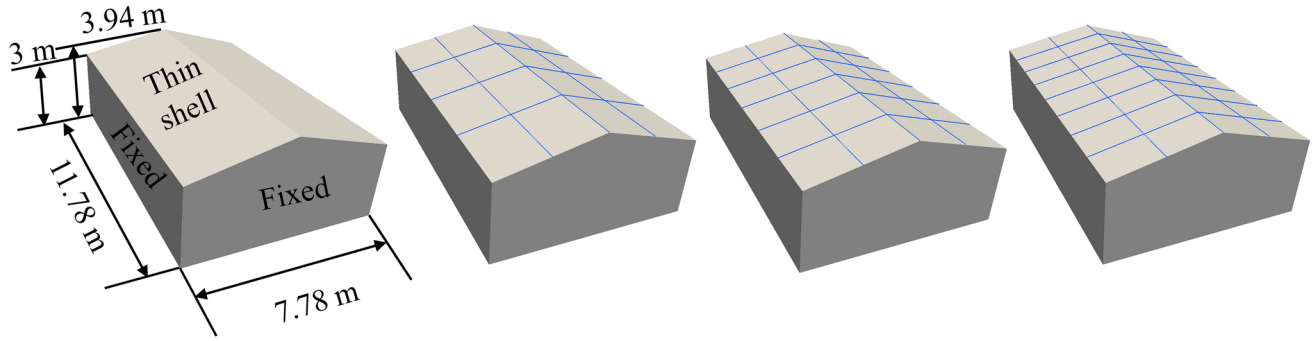

(a) Setup with building (b) 4 × 4 roof panels (c) 4 × 6 roof panels (d) 4 × 8 roof panels

Fig. 2 Geometry and dimensions of the roof

Table 1 Material properties of the roof

Name	Notation (units)	Value
Structure density	ρ_s (kg · m^{-3})	600.0
Young's modulus	E (kg · m^{-2})	3.0×10^9
Poisson's ratio	ν	0.08
Thickness of shell	h (m)	1.111×10^{-2}

the fluid–structure interface. The following boundary conditions (BCs) are employed in the simulations (also see Fig. 4). Dirichlet flow BC based on the wind profile specified in the previous section is used for the inlet, traction-free is used for the outflow, no penetration BC is used for the side and top walls, and no-slip BC is enforced weakly for the fluid–structure interface and the ground. Each roof is simulated with three inflow conditions with turbulent intensity I_r = 5%, 10%, and 20% described above.

Linear eigenvalue analyses are carried out for panels in each roof configuration. Because all the panels are uncoupled in a configuration, the overall roof frequencies are the same as the panel frequencies. The natural frequency of different roof structures changes from 4.28 Hz to 8.20 Hz. Table 2 shows the first 9 mode frequencies of the panels/roofs, while Figs. 5–7 exhibit the mode shapes of a signal panel in each configuration. The low order mode shape, e.g., the mode shape of the first mode, is similar for panels in different configurations, but different mode shapes are observed for the high order modes.

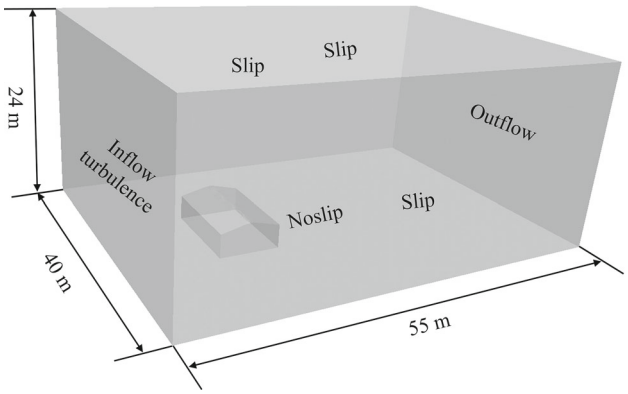

Fig. 4 FSI setup and boundary conditions

4 Results and discussions

The results and discussions are focused on the wind flow field and the aeroelastic effects on pressure coefficients under the

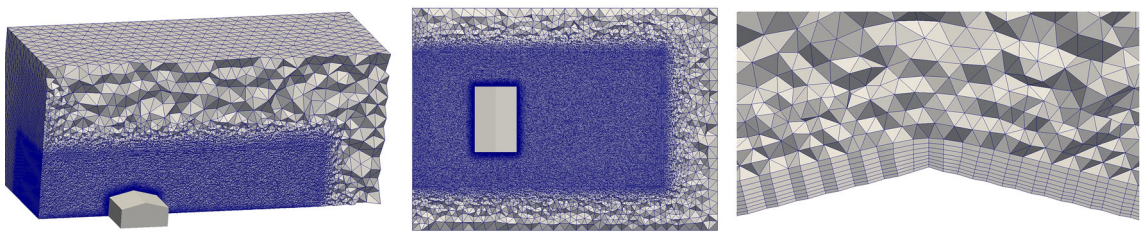

(a) Mesh cut on x-z plane (b) Mesh cut on y-z plane (c) Prism boundary layers

Fig. 3 Fluid mesh of the FSI simulations

Table 2 Mode frequency of roof panels (Hz)

	Configuration		
Mode	4×4	4×6	4×8
1_{st}	4.28	5.91	8.20
2_{nd}	8.21	14.79	17.17
3_{rd}	13.27	14.89	24.14
4_{th}	14.81	23.73	32.28
5_{th}	17.17	29.93	33.02
6_{th}	23.74	30.01	47.99
7_{th}	24.22	38.76	52.05
8_{th}	28.40	38.78	53.79
9_{th}	32.28	51.55	60.70

inflow turbulence intensities and panel configurations specified in the previous sections. The pressure coefficient in this study is defined as

$$C_p = (p - p_\infty)/(\rho U_\infty^2/2) \tag{26}$$

where p_∞ and U_∞ are the characteristic wind pressure and wind speed at the inlet. $\overline{C_p}$ and C_p' denote the time-averaged value of C_p and its standard deviation.

4.1 Wind flow field

Figure 8 shows the time-averaged streamlines and mean velocity magnitude on the plane that 1.0 m above the ground (z = 1.0 m plane) for all analysis cases. Four flow re-circulation regions are observed around the corners of the building envelope due to the flow separation, while additional irregular flow re-circulations are formed behind the building's leeward wall. By comparing the plots in Fig. 8, the turbulence intensity and roof configurations have no significant influence on the size of re-circulation bubbles. However, the variations in turbulence intensity and roof configuration have large impacts on the roof pressure coefficient, which is discussed in the following section.

4.2 Aeroelastic effects

Instantaneous flow fields and roof deflections predicted by the FSI simulations at the fully developed stage are plotted in Fig. 9. As the turbulence intensity increases at the inlet, larger turbulence around the building envelope and in the wake is seen. The turbulence leads to complicated wind-roof interaction and noticeable structural responses. For all three analyzed configurations, the instantaneous displacement magnitude grows with the magnitude of turbulence intensity.

While the time-averaged pressure coefficient, $\overline{C_p}$, provides a baseline for determining the wind load on the roof structure, the pressure fluctuation due to the aeroelastic effects should also beware in the performance based-wind engineering. The standard deviation of the pressure coefficient, C_p', reflects the pressure fluctuation over time.

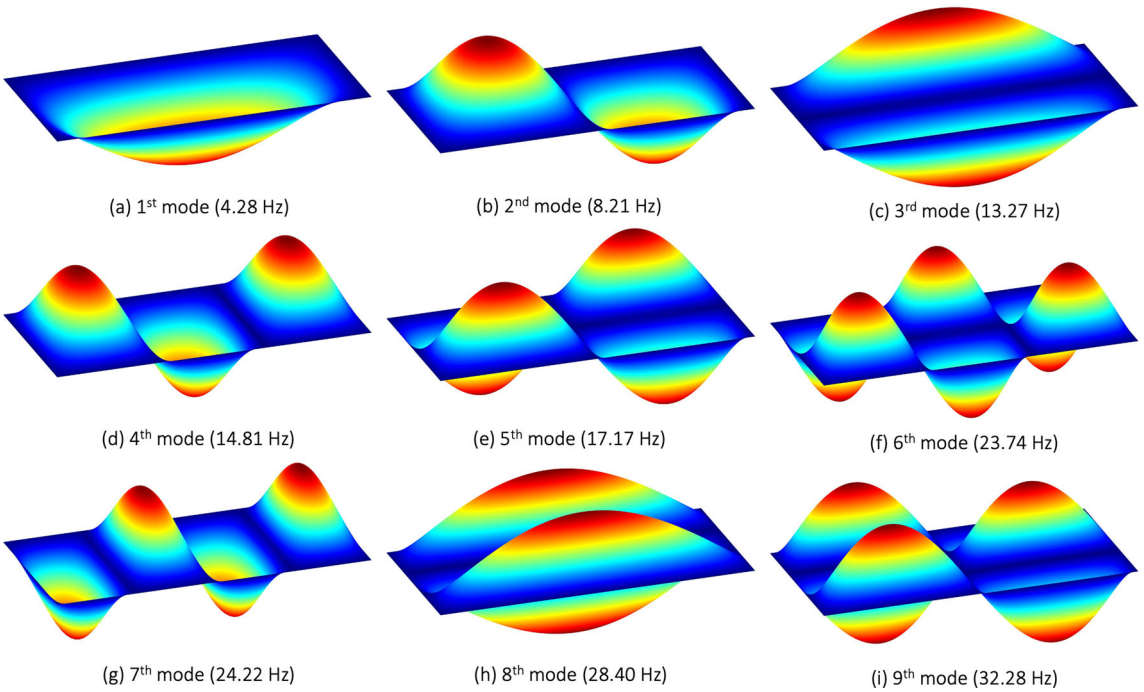

Fig. 5 Mode shapes for a panel from the 4×4 roof configuration

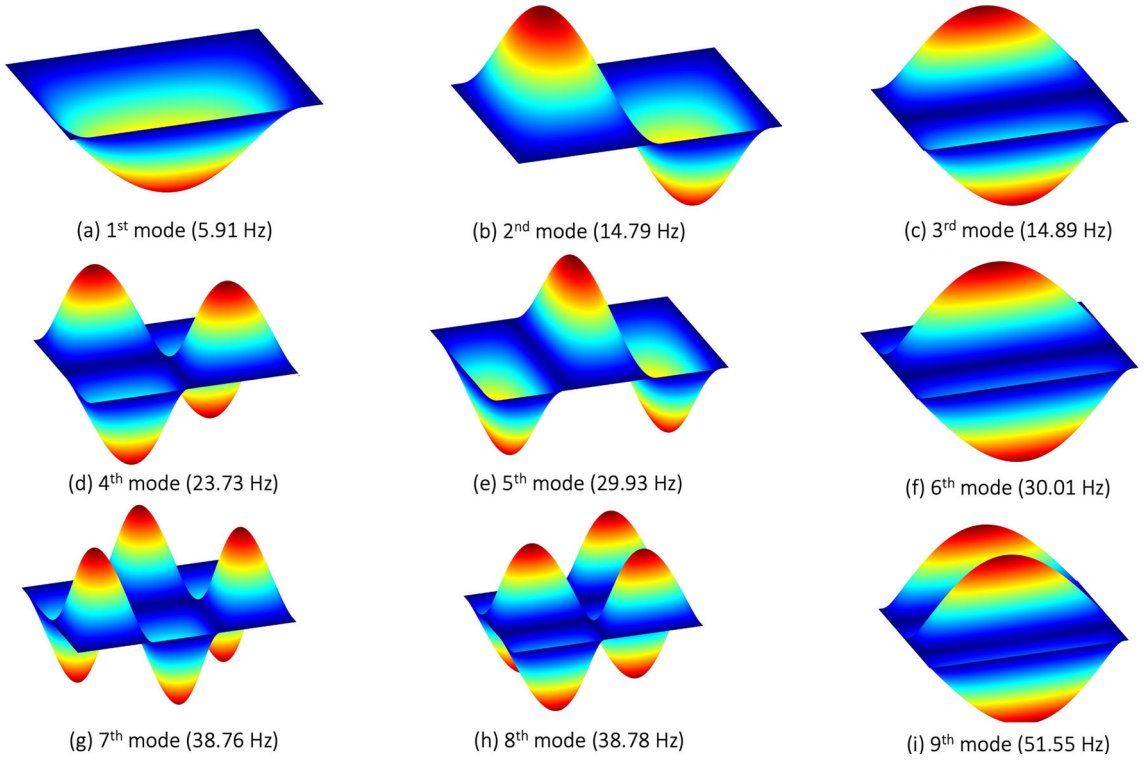

Fig. 6 Mode shapes for a panel from the 4 × 6 roof configuration

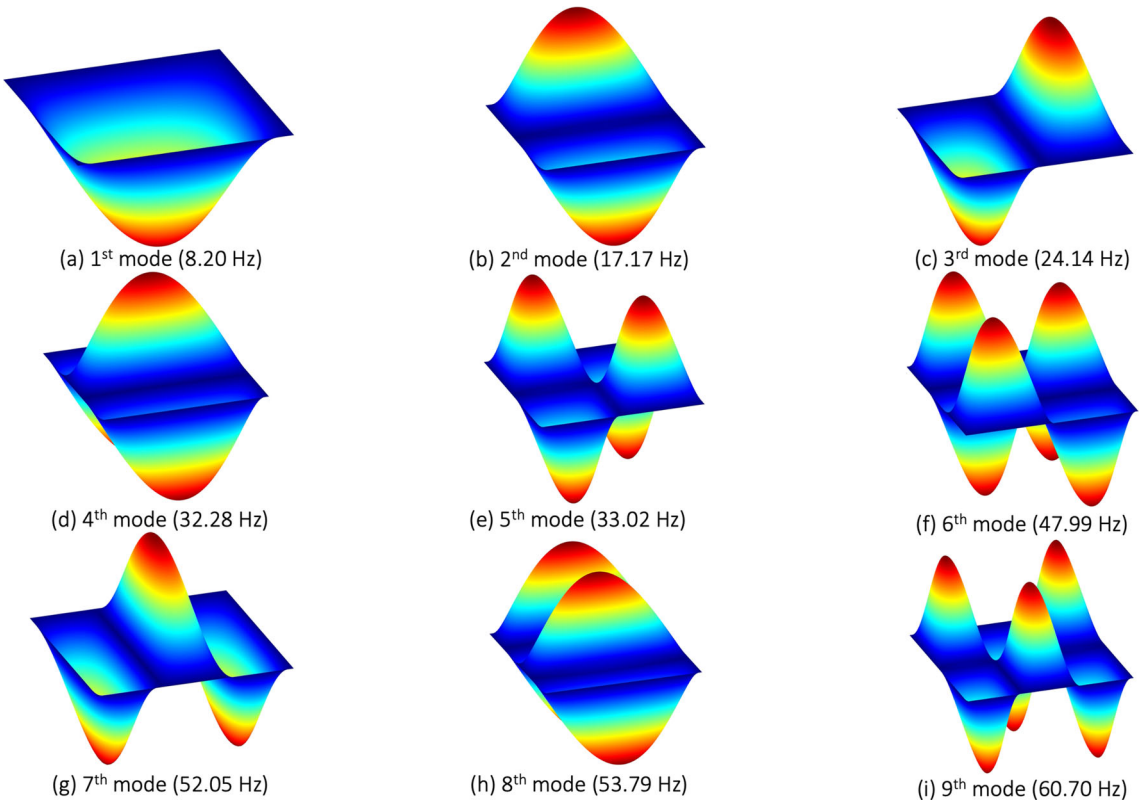

Fig. 7 Mode shapes for a panel from the 4 × 8 roof configuration

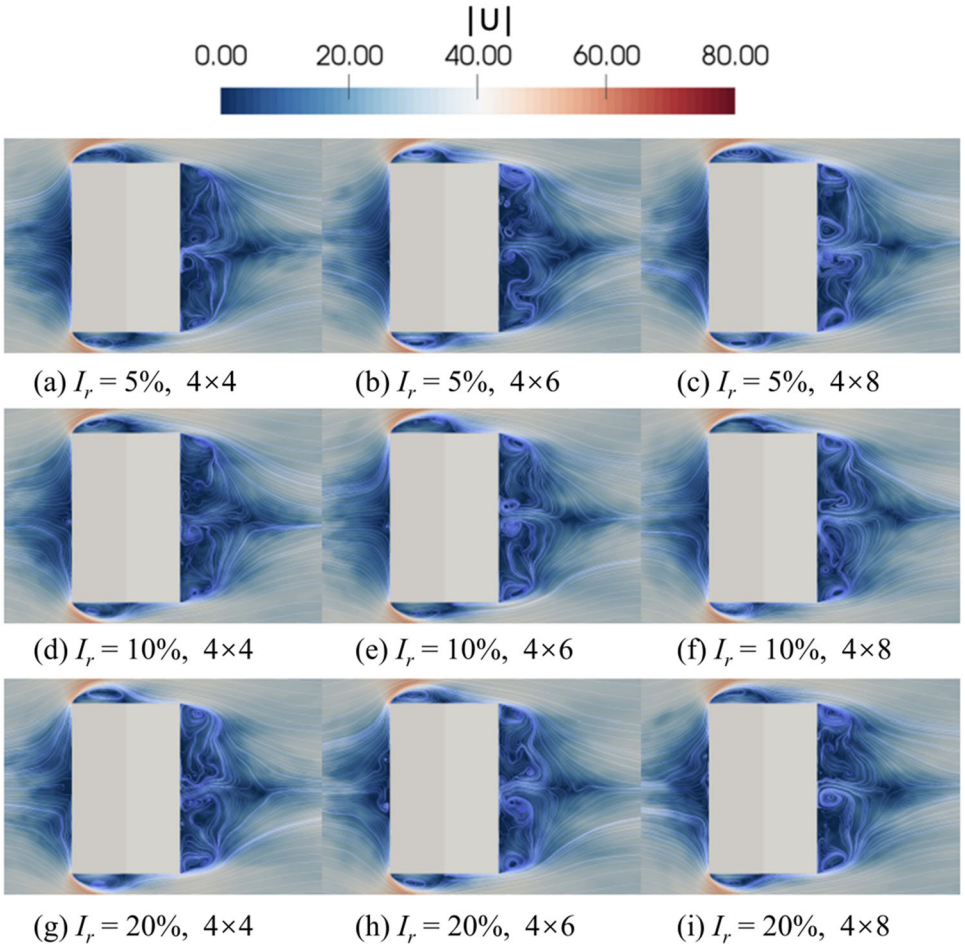

Fig. 8 Time-averaged streamlines and wind speed on the z =1.0 m plane (unit: m/s) t = 7 s

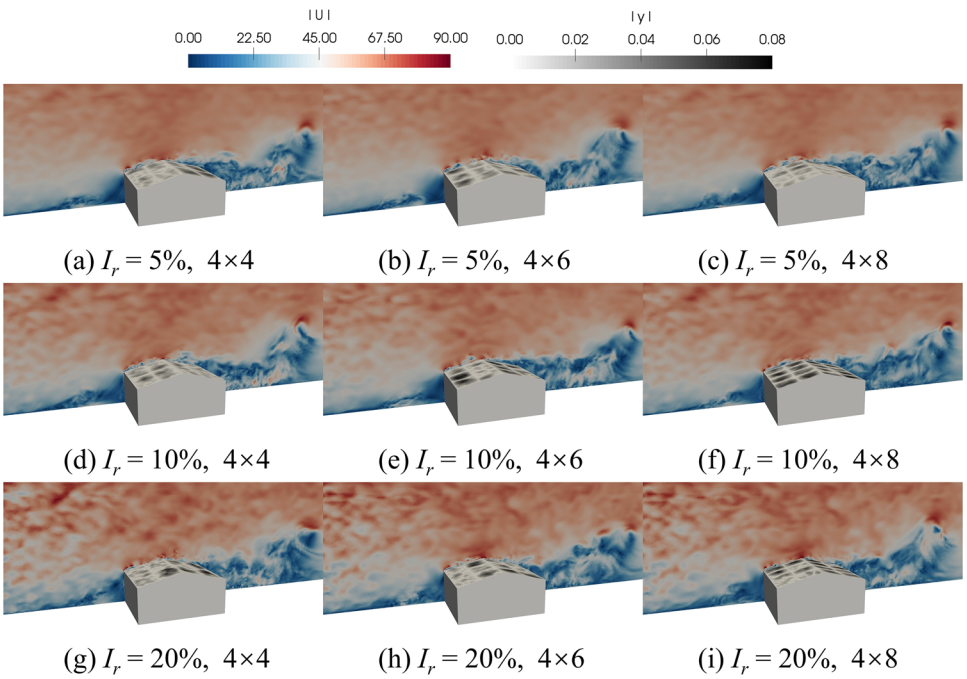

Fig. 9 Instantaneous wind speed (unit: m/s) and roof deformation magnitude (unit: m) at t = 7 s

Fig. 10 $\overline{C_p}$ and C'_p distribution

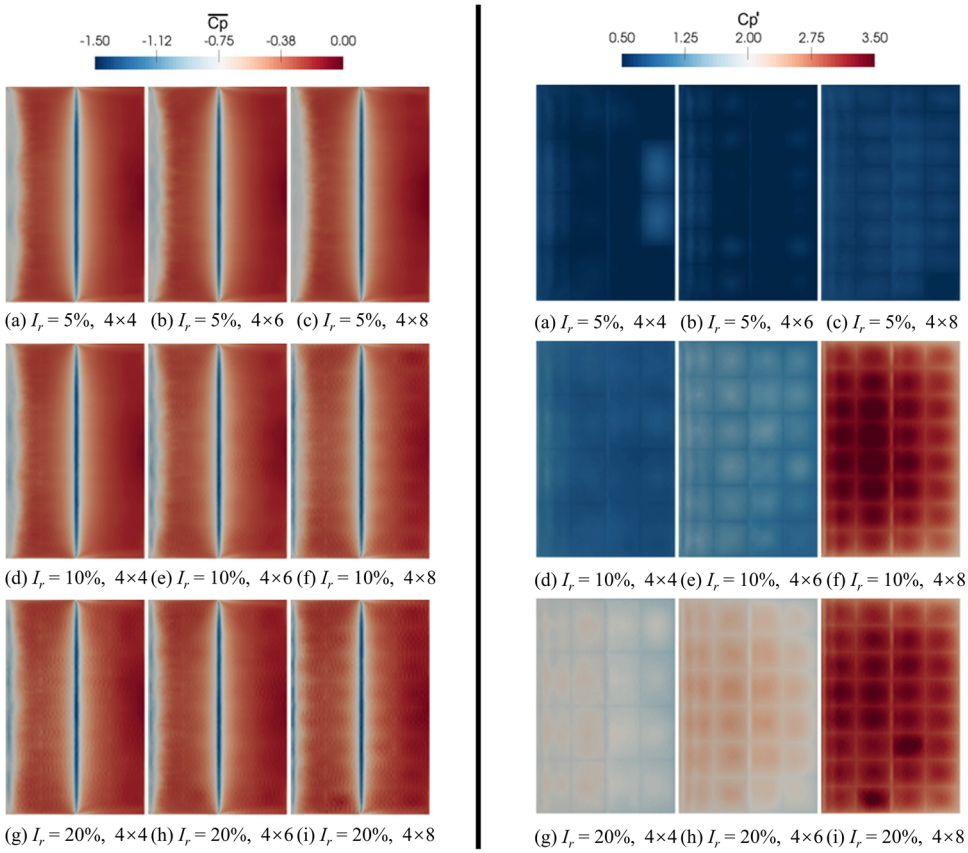

Fig. 11 Diagram of panel center line (marked as red line)

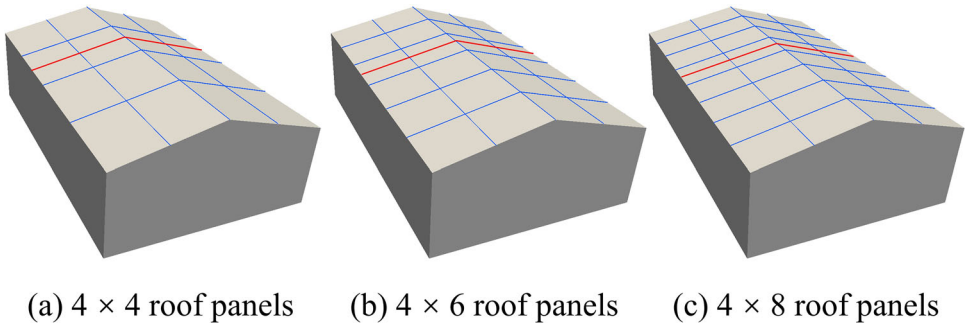

Figure 10 shows distributions of $\overline{C_p}$ and C'_p on the roof structures. The $\overline{C_p}$ and C'_p along the center line of a panel in each configuration (see Fig. 11 for the location) are plotted in Fig. 12 and Fig. 13. All the roof surfaces are subject to high uplift pressure (pressure suction) since the roof slope is relatively small. In particular, the roof windward edge and roof ridge experience larger pressure suctions due to the flow separations in these regions, as shown in Fig. 8 and Fig. 9. The distribution patterns of $\overline{C_p}$ are similar in all cases, as indicated in Fig. 10 (left) and Fig. 12. In contrast, Fig. 10 (right) and Fig. 13 show that the distributions of C'_p over roof panels are significantly different for each case. The value of C'_p increases with the turbulence intensity, I_r, and the overall stiffness of the roof. With the same I_r, the stiffer roof configuration tends to have a larger C'_p, which indicates that the stiffer roof system experiences higher pressure fluctuation due to wind. This effect is also observed in experimental work by [4, 101]. Moreover, it is worth noticing that, for the cases with low I_r (5 %), the difference in pressure fluctuation is not as pronounceable as the cases with higher I_r (10 % and 20 %). For the roof configurations with lower stiffness (4 × 4 and 4 × 6), the increase in pressure fluctuation is proportional to the increment of I_r. However, the increment of C'_p for the roof with the 4 × 8 panel configuration (stiffest configuration in this study) is negligible when I_r goes from 10 % to 20 %. Such behaviors are essential to be considered in the performance based-design process and are difficult to capture without conducting FSI simulations.

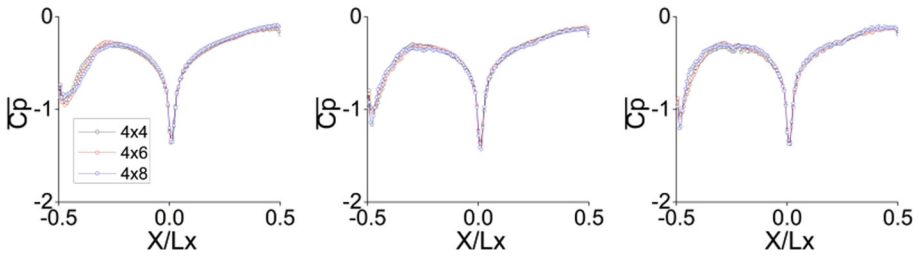

Fig. 12 Comparison of $\overline{C_p}$ over panel center line (I_r = 5 %, 10 %, 20 % from left to right)

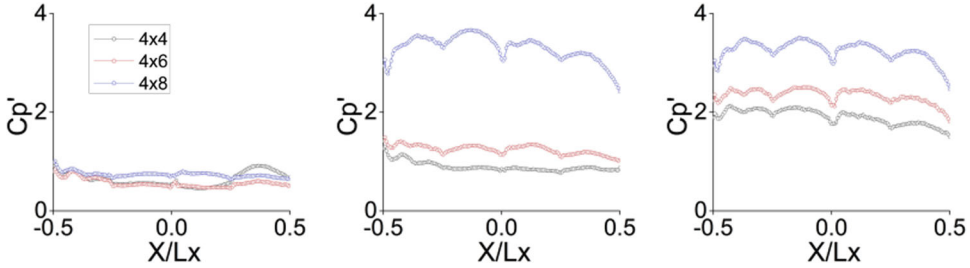

Fig. 13 Comparison of C_p' over panel center line (I_r = 5 %, 10 %, 20 % from left to right)

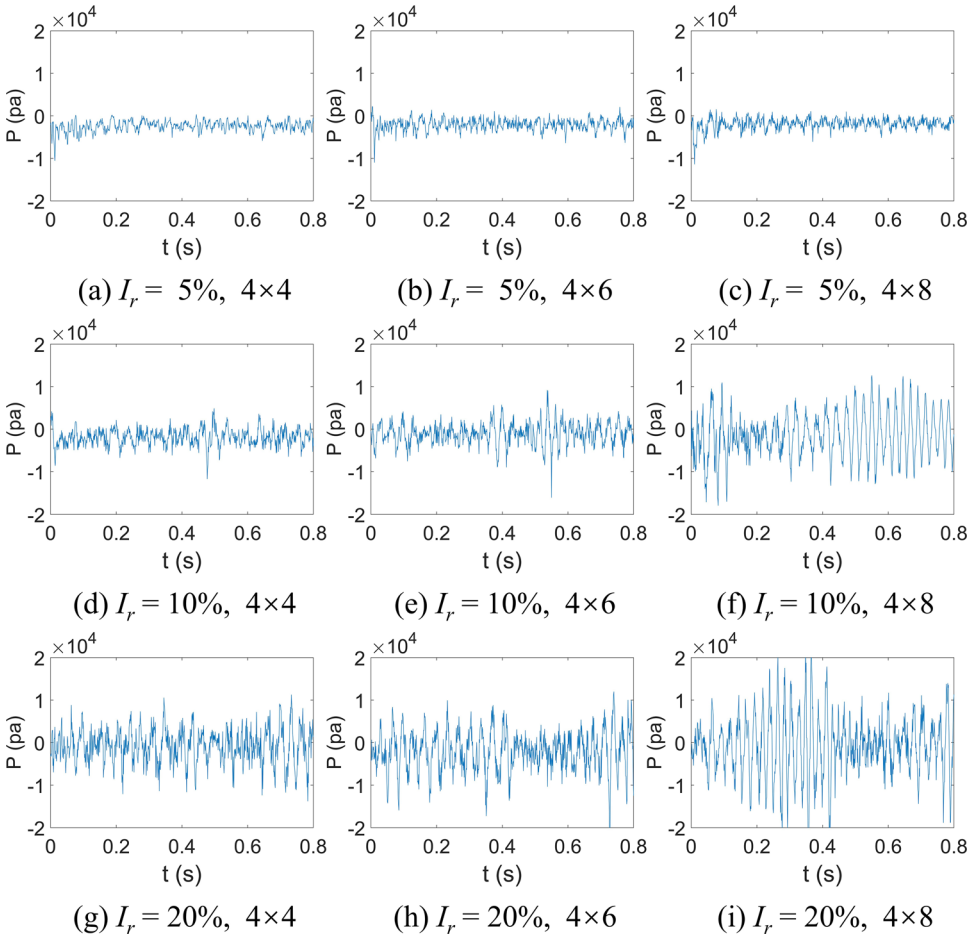

Fig. 14 Time history of wind pressure at a representative location

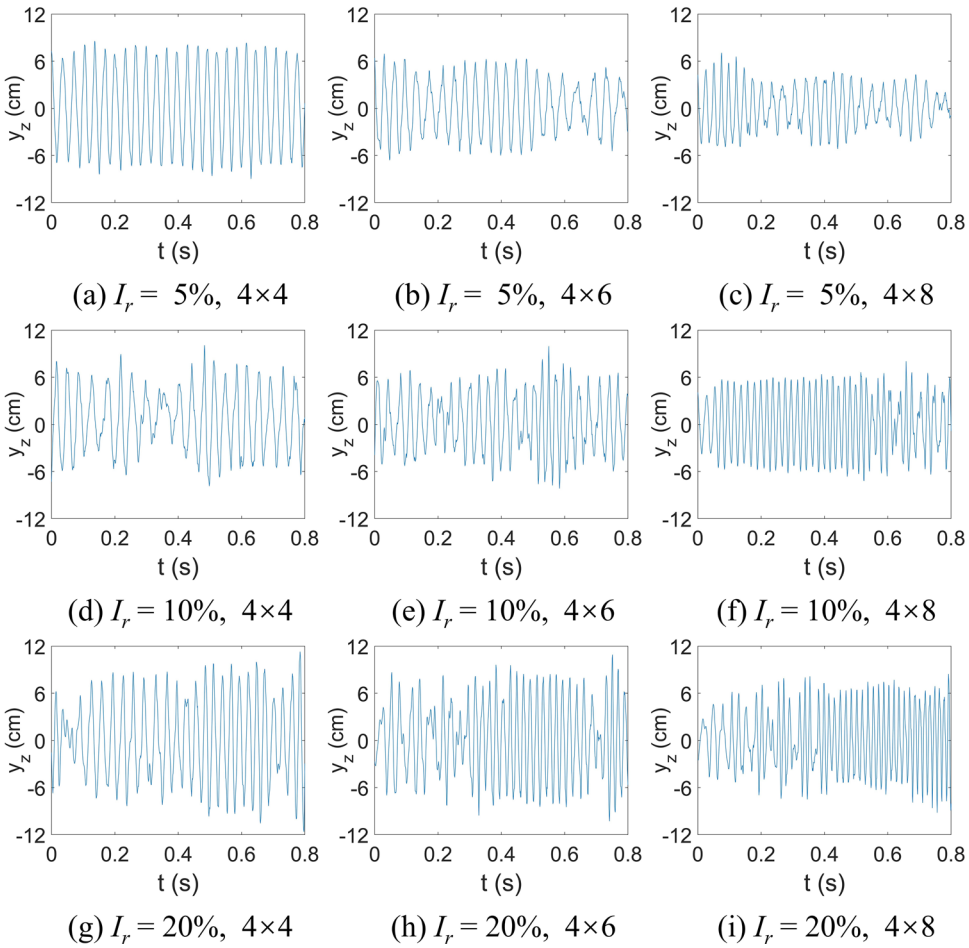

Fig. 15 Time history of deflection at a representative location

To further demonstrate the necessity of FSI simulations, the quasi-steady approach, which is widely used in wind engineering [102–104], is also used for estimating the pressure fluctuations (e.g., standard deviation) and compared with the FSI predictions. The quasi-steady approach is a simplified reduced-order model by ignoring the aeroelastic effects and correlating pressure fluctuation and turbulence intensity based on the following empirical relationship.

$$C'_p \approx 2I_u|\overline{C_p}| \tag{27}$$

where $\overline{C_p}$ is the mean pressure coefficient, which is often estimated based on design codes and standards, for example, ASCE 7-22. The values of $\overline{C_p}$ in ASCE 7-22 are tabulated and can be determined based on the wind load direction, roof angle, and mean roof height to base ratio of the building. For the studied cases, in which the roof angle is 13.58° and the mean roof height to base ratio is 0.446, the value of $\overline{C_p}$ is −0.76. By substitute this value into Eq. 27, values of C'_p for $I_r = 5$, 10, and 20% are 0.076, 0.152, and 0.304, respectively. However, the value of C'_p ranges from 0.5 to 3.5 in the FSI simulation, as shown in Fig. 10 (right) and Fig. 13. In comparison, the pressure fluctuations due to the aeroelastic effects are largely underestimated by the quasi-static approach with the code-based $\overline{C_p}$ value. This discrepancy indicates that the turbulence and aeroelastic behaviors, which lead to large flow separations and structure resonant displacement, have non-negligible effects on pressure fluctuations and should be carefully accounted for in practice.

To illustrate the dynamic process of the wind-roof interaction, a representative location that has the maximum $\overline{C_p}$ is chosen for further analysis. The time history of pressure and roof deflection at this location are plotted in Figs. 14 and 15, respectively. For the pressure coefficient, on the one hand, larger inflow turbulence intensity leads to higher fluctuations for roofs with the same configuration. On the other hand, the pressure fluctuations increase with the number of roof panels (stiffness) under higher turbulence intensity, while the pressure fluctuations stay almost the same in lower turbulence intensity ($I_r = 5$ %). This confirms with the C'_p plots in Fig. 13. For the deflection, for the same roof configuration, increasing inflow turbulence intensity can lead to slightly larger amplitudes in deflection fluctuations. This behavior corresponds to the increasing trend of pressure amplitude presented in Fig. 14. Although, the pressure amplitudes under a I_r condition remain the same or slightly increase when

the number of panels increases, the roof deflection amplitudes reduce due to the increasing overall roof stiffness. It is noteworthy that while the deflection amplitude reduces, the frequencies of deflection fluctuation increase with roof stiffness. This suggests that cyclic fatigue of the roof supporting systems should be carefully considered for structures exposed to high I_r conditions.

5 Conclusion

The paper presented a high-fidelity isogeometric FSI model and its application for investigating the aeroelastic effects on pressure coefficient distributions and deflections of representative roof structures under different wind conditions and roof configurations. The FSI model integrates a set of advanced numerical methods, including moving domain CFD technique-based ALE-VMS and IGA-based Kirchhoff-Love thin shell theory. The simulated results indicated the necessity of FSI simulations under turbulent wind conditions by comparing them with the quasi-steady approach, which significantly underestimates pressure fluctuation. The paper also found that the time-averaged pressure coefficient $\overline{C_p}$ remains almost the same regardless of the turbulent intensity and number of roof panels for a given mean wind profile. At last, the FSI simulations showed that increasing the panel stiffness leads to higher fluctuation in pressure coefficients, which has been evidenced by several experimental investigations. Because increasing the number of roof panels increases the roof stiffness and pressure fluctuation simultaneously, the roof deflection fluctuation seems unchanged for a given inflow turbulence intensity. In addition, the risk of cyclic fatigue due to the increase of deflection fluctuation frequency by increasing overall roof stiffness is demonstrated in the FSI simulation results. Through this case study, we believe that this isogeometric ALE-VMS approach is a valuable FSI tool for wind engineering and structural engineering applications.

Acknowledgements The research was supported by the Center for Infrastructure Resilience in Cities as Livable Environments (CIRCLE) within the ZJU-UIUC Joint Research Program under the Grant of No. DREMES202001.

References

1. Paulotto C, Ciampoli M, Augusti G (2004) Some proposals for a first step towards a performance based wind engineering. IFED Int Forum Eng Decis Mak
2. ASCE/SEI 7-22 (2022) Minimum design loads and associated criteria for buildings and other structures. American Society of Civil Engineers
3. Wood JN, Breuer M, De Nayer G (2018) Experimental studies on the instantaneous fluid-structure interaction of an air-inflated flexible membrane in turbulent flow. J Fluids Struct 80:405–440
4. Estephan J, Feng C, Chowdhury AG, Chavez M, Baskaran A, Moravej M (2021) Characterization of wind-induced pressure on membrane roofs based on full-scale wind tunnel testing. Eng Struct 235:112101
5. Bazilevs Y, Calo VM, Cottrell JA, Hughes TJR, Reali A, Scovazzi G (2007) Variational multiscale residual-based turbulence modeling for large eddy simulation of incompressible flows. Comput Methods Appl Mech Eng 197:173–201
6. Hughes TJR, Cottrell JA, Bazilevs Y (2005) Isogeometric analysis: CAD, finite elements, NURBS, exact geometry, and mesh refinement. Comput Methods Appl Mech Eng 194:4135–4195
7. Cottrell JA, Hughes TJR, Bazilevs Y (2009) Isogeometric analysis. Wiley, Toward Integration of CAD and FEA
8. Hsu M-C, Bazilevs Y (2012) Fluid-structure interaction modeling of wind turbines: simulating the full machine. Comput Mech 50:821–833
9. Yan J, Korobenko A, Deng X, Bazilevs Y (2016) Computational free-surface fluid-structure interaction with application to floating offshore wind turbines. Comput Fluids 141:155–174. https://doi.org/10.1016/j.compfluid.2016.03.008
10. Bazilevs Y, Korobenko A, Deng X, Yan J (2015) Novel structural modeling and mesh moving techniques for advanced FSI simulation of wind turbines. Int J Numer Methods Eng 102:766–783. https://doi.org/10.1002/nme.4738
11. Korobenko A, Hsu M-C, Akkerman I, Bazilevs Y (2013) Aerodynamic simulation of vertical-axis wind turbines. J Appl Mech 81:021011. https://doi.org/10.1115/1.4024415
12. Benson D, Bazilevs Y, Hsu M, Hughes T (2011) A large deformation, rotation-free, isogeometric shell. Comput Methods Appl Mech Eng 200(13–16):1367–1378
13. Brooks AN, Hughes TJR (1982) Streamline upwind/Petrov–Galerkin formulations for convection dominated flows with particular emphasis on the incompressible Navier-Stokes equations. Comput Methods Appl Mech Eng 32:199–259
14. Tezduyar TE (1992) Stabilized finite element formulations for incompressible flow computations. Adv Appl Mech 28:1–44. https://doi.org/10.1016/S0065-2156(08)70153-4
15. Hughes TJR, Franca LP, Hulbert GM (1989) A new finite element formulation for computational fluid dynamics: VIII. The Galerkin/least-squares method for advective-diffusive equations. Comput Methods Appl Mech Eng 73:173–189
16. Bazilevs Y, Hsu M-C, Scott MA (2012) Isogeometric fluid-structure interaction analysis with emphasis on non-matching discretizations, and with application to wind turbines. Comput Methods Appl Mech Eng 249–252:28–41
17. Tezduyar TE, Sathe S, Keedy R, Stein K (2006) Space-time finite element techniques for computation of fluid-structure interactions. Comput Methods Appl Mech Eng 195:2002–2027. https://doi.org/10.1016/j.cma.2004.09.014
18. Tezduyar TE, Sathe S (2007) Modeling of fluid-structure interactions with the space-time finite elements: solution techniques. Int J Numer Methods Fluids 54:855–900. https://doi.org/10.1002/fld.1430
19. Bazilevs Y, Hughes TJR (2007) Weak imposition of Dirichlet boundary conditions in fluid mechanics. Comput Fluids 36:12–26
20. Cen H, Zhou Q, Korobenko A (2022) Wall-function-based weak imposition of Dirichlet boundary condition for stratified turbulent flows. Comput Fluids 234:105257
21. Herrema AJ, Johnson EL, Proserpio D, Wu MCH, Kiendl J, Hsu M-C (2019) Penalty coupling of non-matching isogeometric Kirchhoff-Love shell patches with application to composite wind turbine blades. Comput Methods Appl Mech Eng 346:810–840
22. Kamensky D, Xu F, Lee C, Yan J, Bazilevs Y, Hsu M (2018) A contact formulation based on a volumetric potential: application

to isogeometric simulations of atrioventricular valves. Comput Methods Appl Mech Eng 330:522–546
23. Terahara T, Takizawa K, Tezduyar TE (2023) T-splines computational membrane-cable structural mechanics with continuity and smoothness: I. Method Implement Comput Mech 71:657–675. https://doi.org/10.1007/s00466-022-02256-w
24. Terahara T, Takizawa K, Avsar R, Tezduyar TE (2023) T-splines computational membrane-cable structural mechanics with continuity and smoothness: II. Spacecraft Parachutes Comput Mech 71:677–686. https://doi.org/10.1007/s00466-022-02265-9
25. Taniguchi Y, Takizawa K, Otoguro Y, Tezduyar T (2022) A hyperelastic extended Kirchhoff-Love shell model with out-of-plane normal stress: I. Out-of-plane deformation. Comput Mech 70(2):247–280
26. Zhu Q, Zhu M, Yan J (2022) Isogeometric large-eddy simulations of turbulent particle-laden flows. Math Models Methods Appl Sci 32(12):2529–2550. https://doi.org/10.1142/S0218202522500609
27. Rajanna MR, Johnson EL, Liu N, Korobenko A, Bazilevs Y, Hsu M-C (2022) Fluid-structure interaction modeling with nonmatching interface discretizations for compressible flow problems: computational framework and validation study. Math Models Methods Appl Sci 32(12):2497–2528. https://doi.org/10.1142/S0218202522500592
28. Shende S, Behzadinasab M, Moutsandis G, Bazilevs Y (2022) Simulating air blast on concrete structures using the volumetric penalty coupling of isogeometric analysis and peridynamics. Math Models Methods Appl Sci 32(12):2477–2496. https://doi.org/10.1142/S0218202522500580
29. Kuraishi T, Takizawa K, Tezduyar TE (2022) Boundary layer mesh resolution in flow computation with the space-time variational multiscale method and isogeometric discretization. Math Mod Methods Appl Sci 32(12):2401–2443. https://doi.org/10.1142/S0218202522500567
30. Cen H, Zhou Q, Korobenko A (2022) Isogeometric variational multiscale modeling of stably stratified flow over complex terrains. Math Mod Methods Appl Sci 32(12):2371–2399. https://doi.org/10.1142/S0218202522500555
31. Liu Y, Takizawa K, Tezduyar TE, Kuraishi T, Zhang Y (2022) Carrier-domain method for high-resolution computation of time-periodic long-wake flows. Comput Mech 71:169–190. https://doi.org/10.1007/s00466-022-02230-6
32. Bazilevs Y, Calo VM, Hughes TJR, Zhang Y (2008) Isogeometric fluid-structure interaction: theory, algorithms, and computations. Comput Mech 43:3–37
33. Takizawa K, Bazilevs Y, Tezduyar TE (2012) Space-time and ALE-VMS techniques for patient-specific cardiovascular fluid-structure interaction modeling. Arch Comput Methods Eng 19:171–225. https://doi.org/10.1007/s11831-012-9071-3
34. Bazilevs Y, Hsu M-C, Takizawa K, Tezduyar TE (2012) ALE-VMS and ST-VMS methods for computer modeling of wind-turbine rotor aerodynamics and fluid-structure interaction. Math Models Methods Appl Sci 22(02):1230002. https://doi.org/10.1142/S0218202512300025
35. Bazilevs Y, Takizawa K, Tezduyar TE (2013) Computational fluid-structure interaction: methods and applications. Wiley. https://doi.org/10.1002/9781118483565
36. Bazilevs Y, Takizawa K, Tezduyar TE (2013) Challenges and directions in computational fluid-structure interaction. Math Mod Methods Appl Sci 23:215–221. https://doi.org/10.1142/S0218202513400010
37. Bazilevs Y, Takizawa K, Tezduyar TE (2015) New directions and challenging computations in fluid dynamics modeling with stabilized and multiscale methods. Math Mod Methods Appl Sci 25:2217–2226. https://doi.org/10.1142/S0218202515020029
38. Bazilevs Y, Takizawa K, Tezduyar TE (2019) Computational analysis methods for complex unsteady flow problems. Math Mod Methods Appl Sci 29:825–838. https://doi.org/10.1142/S0218202519020020
39. Takizawa K, Tezduyar TE (2012) Computational methods for parachute fluid-structure interactions. Arch Comput Methods Eng 19:125–169. https://doi.org/10.1007/s11831-012-9070-4
40. Takizawa K, Fritze M, Montes D, Spielman T, Tezduyar TE (2012) Fluid-structure interaction modeling of ringsail parachutes with disreefing and modified geometric porosity. Comput Mech 50:835–854. https://doi.org/10.1007/s00466-012-0761-3
41. Takizawa K, Tezduyar TE, Boben J, Kostov N, Boswell C, Buscher A (2013) Fluid-structure interaction modeling of clusters of spacecraft parachutes with modified geometric porosity. Comput Mech 52:1351–1364. https://doi.org/10.1007/s00466-013-0880-5
42. Takizawa K, Tezduyar TE, Boswell C, Tsutsui Y, Montel K (2015) Special methods for aerodynamic-moment calculations from parachute FSI modeling. Comput Mech 55:1059–1069. https://doi.org/10.1007/s00466-014-1074-5
43. Kalro V, Tezduyar TE (2000) A parallel 3D computational method for fluid-structure interactions in parachute systems. Comput Methods Appl Mech Eng 190:321–332. https://doi.org/10.1016/S0045-7825(00)00204-8
44. Kuraishi T, Yamasaki S, Takizawa K, Tezduyar TE, Xu Z, Kaneko R (2022) Space-time isogeometric analysis of car and tire aerodynamics with road contact and tire deformation and rotation. Comput Mech 70(1):49–72
45. Takizawa K, Bazilevs Y, Tezduyar T (2022) Mesh moving methods in flow computations with the space-time and arbitrary Lagrangian–Eulerian methods. J Adv Eng Comput 6(85):112
46. Zhu Q, Yan J, Tejada-Martínez A, Bazilevs Y (2020) Variational multiscale modeling of langmuir turbulent boundary layers in shallow water using isogeometric analysis. Mech Res Commun 108:103570. https://doi.org/10.1016/j.mechrescom.2020.103570
47. Ravensbergen M, Helgedagsrud TA, Bazilevs Y, Korobenko A (2020) A variational multiscale framework for atmospheric turbulent flows over complex environmental terrains. Comput Methods Appl Mech Eng 368:113182. https://doi.org/10.1016/j.cma.2020.113182
48. Yan J, Korobenko A, Tejada-Martinez AE, Golshan R, Bazilevs Y (2017) A new variational multiscale formulation for stratified incompressible turbulent flows. Comput Fluids 158:150–156. https://doi.org/10.1016/j.compfluid.2016.12.004
49. Bazilevs Y, Hsu M-C, Akkerman I, Wright S, Takizawa K, Henicke B, Spielman T, Tezduyar TE (2011) 3D simulation of wind turbine rotors at full scale. Part I: geometry modeling and aerodynamics. Int J Numer Methods Fluids 65:207–235. https://doi.org/10.1002/fld.2400
50. Takizawa K, Henicke B, Tezduyar TE, Hsu M-C, Bazilevs Y (2011) Stabilized space-time computation of wind-turbine rotor aerodynamics. Comput Mech 48:333–344. https://doi.org/10.1007/s00466-011-0589-2
51. Takizawa K, Henicke B, Montes D, Tezduyar TE, Hsu M-C, Bazilevs Y (2011) Numerical-performance studies for the stabilized space-time computation of wind-turbine rotor aerodynamics. Computat Mech 48:647–657. https://doi.org/10.1007/s00466-011-0614-5
52. Takizawa K, Tezduyar TE, McIntyre S, Kostov N, Kolesar R, Habluetzel C (2014) Space-time VMS computation of wind-turbine rotor and tower aerodynamics. Computat Mech 53:1–15. https://doi.org/10.1007/s00466-013-0888-x
53. Takizawa K, Bazilevs Y, Tezduyar TE, Hsu M-C, Øiseth O, Mathisen KM, Kostov N, McIntyre S (2014) Engineering analysis and design with ALE-VMS and space-time methods. Arch Com-

put Methods Eng 21:481–508. https://doi.org/10.1007/s11831-014-9113-0
54. Takizawa K (2014) Computational engineering analysis with the new-generation space-time methods. Comput Mech 54:193–211. https://doi.org/10.1007/s00466-014-0999-z
55. Bazilevs Y, Takizawa K, Tezduyar TE, Hsu M-C, Kostov N, McIntyre S (2014) Aerodynamic and FSI analysis of wind turbines with the ALE-VMS and ST-VMS methods. Arch Comput Methods Eng 21:359–398. https://doi.org/10.1007/s11831-014-9119-7
56. Takizawa K, Tezduyar TE, Mochizuki H, Hattori H, Mei S, Pan L, Montel K (2015) Space-time VMS method for flow computations with slip interfaces (ST-SI). Math Mod Methods Appl Sci 25:2377–2406. https://doi.org/10.1142/S0218202515400126
57. Otoguro Y, Mochizuki H, Takizawa K, Tezduyar TE (2020) Space-time variational multiscale isogeometric analysis of a tsunami-shelter vertical-axis wind turbine. Comput Mech 66:1443–1460. https://doi.org/10.1007/s00466-020-01910-5
58. Ravensbergen M, Bayram AM, Korobenko A (2020) The actuator line method for wind turbine modelling applied in a variational multiscale framework. Comput Fluids 201:104465. available online. https://doi.org/10.1016/j.compfluid.2020.104465
59. Bazilevs Y, Korobenko A, Deng X, Yan J, Kinzel M, Dabiri JO (2014) FSI modeling of vertical-axis wind turbines. J Appl Mech 81:081006. https://doi.org/10.1115/1.4027466
60. Korobenko A, Bazilevs Y, Takizawa K, Tezduyar TE (2018) Recent advances in ALE-VMS and ST-VMS computational aerodynamic and FSI analysis of wind turbines. In: Tezduyar TE (ed), Frontiers in computational fluid–structure interaction and flow simulation: research from lead investigators under forty – 2018, Modeling and Simulation in Science, Engineering and Technology, Springer, pp. 253–336. https://doi.org/10.1007/978-3-319-96469-0_7
61. Korobenko A, Bazilevs Y, Takizawa K, Tezduyar TE (2019) Computer modeling of wind turbines: 1. ALE-VMS and ST-VMS aerodynamic and FSI analysis. Arch Comput Methods Eng 26:1059–1099. https://doi.org/10.1007/s11831-018-9292-1
62. Bayram AM, Bear C, Bear M, Korobenko A (2020) Performance analysis of two vertical-axis hydrokinetic turbines using variational multiscale method. Comput Fluids 200:104432. available online. https://doi.org/10.1016/j.compfluid.2020.104432
63. Yan J, Deng X, Xu F, Xu S, Zhu Q. Numerical simulations of two back-to-back horizontal axis tidal stream turbines in free-surface flows. J Appl Mech 87 (6). https://doi.org/10.1115/1.4046317
64. Kuraishi T, Zhang F, Takizawa K, Tezduyar TE (2021) Wind turbine wake computation with the ST-VMS method, isogeometric discretization and multidomain method: I. Computational framework. Comput Mech 68(1):113–130
65. Kuraishi T, Zhang F, Takizawa K, Tezduyar TE (2021) Wind turbine wake computation with the ST-VMS method, isogeometric discretization and multidomain method: II. Spatial and temporal resolution. Comput Mech 68(1):175–184
66. Ravensbergen M, Mohamed A, Korobenko A (2020) The actuator line method for wind turbine modelling applied in a variational multiscale framework. Comput Fluids 201:104465
67. Mohamed A, Bear C, Bear M, Korobenko A (2020) Performance analysis of two vertical-axis hydrokinetic turbines using variational multiscale method. Comput Fluids 200:104432
68. Bayram A, Korobenko A (2020) Variational multiscale framework for cavitating flows. Comput Mech, pp 1–19
69. Yan J, Deng X, Korobenko A, Bazilevs Y (2017) Free-surface flow modeling and simulation of horizontal-axis tidal-stream turbines. Comput Fluids 158:157–166. https://doi.org/10.1016/j.compfluid.2016.06.016
70. Zhu Q, Yan J (2021) A moving-domain CFD solver in FEniCS with applications to tidal turbine simulations in turbulent flows. Comput Math Appl 81:532–546
71. Bayram AM, Korobenko A (2020) Variational multiscale framework for cavitating flows. Comput Mech 66:49–67. https://doi.org/10.1007/s00466-020-01840-2
72. Bayram A, Korobenko A (2021) A numerical formulation for cavitating flows around marine propellers based on variational multiscale method. Comput Mech 68(2):405–432
73. Codoni D, Moutsanidis G, Hsu M-C, Bazilevs Y, Johansen C, Korobenko A (2021) Stabilized methods for high-speed compressible flows: toward hypersonic simulations. Comput Mech 67:785–809. https://doi.org/10.1007/s00466-020-01963-6
74. Terahara T, Takizawa K, Tezduyar TE, Bazilevs Y, Hsu M-C (2020) Heart valve isogeometric sequentially-coupled FSI analysis with the space-time topology change method. Comput Mech 65:1167–1187. https://doi.org/10.1007/s00466-019-01813-0
75. Hsu M-C, Kamensky D, Bazilevs Y, Sacks MS, Hughes TJR (2014) Fluid-structure interaction analysis of bioprosthetic heart valves: significance of arterial wall deformation. Comput Mech 54:1055–1071. https://doi.org/10.1007/s00466-014-1059-4
76. Johnson EL, Wu MCH, Xu F, Wiese NM, Rajanna MR, Herrema AJ, Ganapathysubramanian B, Hughes TJR, Sacks MS, Hsu M-C (2020) Thinner biological tissues induce leaflet flutter in aortic heart valve replacements. Proc Nat Acad Sci 117:19007–19016
77. Takizawa K, Bazilevs Y, Tezduyar TE, Hsu M-C (2019) Computational cardiovascular flow analysis with the variational multiscale methods. J Adv Eng Comput 3:366–405. https://doi.org/10.25073/jaec.201932.245
78. Kuraishi T, Terahara T, Takizawa K, Tezduyar T (2022) Computational flow analysis with boundary layer and contact representation: I. Tire aerodynamics with road contact. J Mech 38:77–87
79. Terahara T, Kuraishi T, Takizawa K, Tezduyar T (2022) Computational flow analysis with boundary layer and contact representation: II. Heart valve flow with leaflet contact. J Mech 38:185–194
80. Takizawa K, Bazilevs Y, Tezduyar TE, Hsu M, Terahara T (2022) Computational cardiovascular medicine with isogeometric analysis. J Adv Eng Comput 6(3):167–199
81. Otoguro Y, Takizawa K, Tezduyar TE, Nagaoka K, Avsar R, Zhang Y (2019) Space-time VMS flow analysis of a turbocharger turbine with isogeometric discretization: computations with time-dependent and steady-inflow representations of the intake/exhaust cycle. Comput Mech 64:1403–1419. https://doi.org/10.1007/s00466-019-01722-2
82. Otoguro Y, Takizawa K, Tezduyar TE, Nagaoka K, Mei S (2019) Turbocharger turbine and exhaust manifold flow computation with the space-time variational multiscale method and isogeometric analysis. Comput Fluids 179:764–776. https://doi.org/10.1016/j.compfluid.2018.05.019
83. Xu F, Moutsanidis G, Kamensky D, Hsu M-C, Murugan M, Ghoshal A, Bazilevs Y (2017) Compressible flows on moving domains: stabilized methods, weakly enforced essential boundary conditions, sliding interfaces, and application to gas-turbine modeling. Comput Fluids 158:201–220. https://doi.org/10.1016/j.compfluid.2017.02.006
84. Takizawa K, Tezduyar TE, Kuraishi T (2015) Multiscale ST methods for thermo-fluid analysis of a ground vehicle and its tires. Math Mod Methods Appl Sci 25:2227–2255. https://doi.org/10.1142/S0218202515400072
85. Kuraishi T, Takizawa K, Tabata S, Asada S, Tezduyar TE (2014) Multiscale thermo-fluid analysis of a tire. In: Proceedings of the 19th Japan society of computational engineering and science conference, Hiroshima, Japan
86. Kuraishi T, Takizawa K, Tezduyar TE (2018) Space–time computational analysis of tire aerodynamics with actual geometry, road contact and tire deformationIn: Tezduyar TE (ed.), Frontiers in computational fluid–structure interaction and flow simulation: research from lead investigators under forty—2018, Modeling and

Simulation in Science, Engineering and Technology, Springer, pp 337–376. https://doi.org/10.1007/978-3-319-96469-0_8
87. Kuraishi T, Takizawa K, Tezduyar TE (2019) Tire aerodynamics with actual tire geometry, road contact and tire deformation. Comput Mech 63:1165–1185. https://doi.org/10.1007/s00466-018-1642-1
88. Kuraishi T, Takizawa K, Tezduyar TE (2019) Space-time computational analysis of tire aerodynamics with actual geometry, road contact, tire deformation, road roughness and fluid film. Comput Mech 64:1699–1718. https://doi.org/10.1007/s00466-019-01746-8
89. Kuraishi T, Xu Z, Takizawa K, Tezduyar T, Yamasaki S (2022) High-resolution multi-domain space-time isogeometric analysis of car and tire aerodynamics with road contact and tire deformation and rotation. Comput Mech 70(6):1257–1279
90. Chung YM, Sung HJ (1997) Comparative study of inflow conditions for spatially evolving simulation. AIAA J 35(2):269–274
91. Yang XI, Meneveau C (2016) Recycling inflow method for simulations of spatially evolving turbulent boundary layers over rough surfaces. J Turbulence 17(1):75–93
92. Stolz S, Adams NA (2003) Large-eddy simulation of high-Reynolds-number supersonic boundary layers using the approximate deconvolution model and a rescaling and recycling technique. Phys Fluids 15(8):2398–2412
93. Morgan B, Larsson J, Kawai S, Lele SK (2011) Improving low-frequency characteristics of recycling/rescaling inflow turbulence generation. AIAA J 49(3):582–597
94. Pamiès M, Weiss P-E, Garnier E, Deck S, Sagaut P (2009) Generation of synthetic turbulent inflow data for large eddy simulation of spatially evolving wall-bounded flows. Phys Fluids 21(4):045103
95. Shur ML, Spalart PR, Strelets MK, Travin AK (2014) Synthetic turbulence generators for rans-les interfaces in zonal simulations of aerodynamic and aeroacoustic problems. Flow Turbulence Combustion 93(1):63–92
96. Poletto R, Craft T, Revell A (2013) A new divergence free synthetic eddy method for the reproduction of inlet flow conditions for LES. Flow Turbulence Combustion 91(3):519–539
97. Kraichnan RH (1970) Diffusion by a random velocity field. Phys Fluids 13(1):22–31
98. Bechara W, Bailly C, Lafon P, Candel SM (1994) Stochastic approach to noise modeling for free turbulent flows. AIAA J 32(3):455–463
99. Jarrin N, Benhamadouche S, Laurence D, Prosser R (2006) A synthetic-eddy-method for generating inflow conditions for large-eddy simulations. Int J Heat Fluid Flow 27(4):585–593
100. Jarrin N, Prosser R, Uribe J-C, Benhamadouche S, Laurence D (2009) Reconstruction of turbulent fluctuations for hybrid RANS/LES simulations using a synthetic-eddy method. Int J Heat Fluid Flow 30(3):435–442
101. Li T, Yang Q, Ishihara T (2018) Unsteady aerodynamic characteristics of long-span roofs under forced excitation. J Wind Eng Ind Aerodyn 181:46–60
102. Kawai H (1983) Pressure fluctuations on square prisms-applicability of strip and quasi-steady theories. J Wind Eng Ind Aerodyn 13(1–3):197–208
103. Letchford CW, Iverson RE, McDonald JR (1993) The application of the quasi-steady theory to full scale measurements on the texas tech building. J Wind Eng Ind Aerodyn 48(1):111–132
104. Richards PJ, Hoxey RP, Wanigaratne BS (1995) The effect of directional variations on the observed mean and rms pressure coefficients. J Wind Eng Ind Aerodyn 54:359–367